

Determination of the isotopic change in nuclear charge radius from extreme-ultraviolet spectroscopy of highly charged ions of Xe

R. Silwal,^{1,2,*} A. Lapierre,³ J. D. Gillaspay,^{2,4} J. M. Dreiling,^{2,†} S. A. Blundell,⁵ Dipti ,² A. Borovik, Jr. ,^{2,‡} G. Gwinner ,⁶ A. C. C. Villari,³ Yu. Ralchenko ,² and E. Takacs ,^{1,2}

¹*Department of Physics and Astronomy, Clemson University, Clemson, South Carolina 29634, USA*

²*National Institute of Standards and Technology, Gaithersburg, Maryland 20899, USA*

³*National Superconducting Cyclotron Laboratory, Michigan State University, East Lansing, Michigan 48824, USA*

⁴*National Science Foundation, Alexandria, Virginia 22314, USA*

⁵*Université Grenoble Alpes, CEA, CNRS, IRIG, SyMMES, 38000 Grenoble, France*

⁶*Department of Physics and Astronomy, University of Manitoba, Winnipeg, Manitoba, Canada R3T 2N2*



(Received 11 March 2020; accepted 22 May 2020; published 16 June 2020)

The electron-beam ion trap (EBIT) at the National Institute of Standards and Technology (NIST) was employed for the measurement and detailed analysis of the $\delta\lambda(^{124}\text{Xe}, ^{136}\text{Xe})$ isotopic shifts of the Al-like $3s^2 3p \ ^2P_{1/2}-3s^2 3p \ ^2P_{3/2}$, Al-like $3s^2 3p \ ^2P_{1/2}-3s^2 3d \ ^2D_{3/2}$, Mg-like $3s^2 \ ^1S_0-3s3p \ ^1P_1$, Mg-like $3s^2 \ ^1S_0-3s3p \ ^3P_1$, Na-like $3s \ ^2S_{1/2}-3p \ ^2P_{1/2}$ (D_1), and Na-like $3s \ ^2S_{1/2}-3p \ ^2P_{3/2}$ (D_2) transitions. Systematic analysis revealed possible line blends and contributing experimental uncertainties. Highly accurate atomic-structure calculations were conducted and used to determine the $\delta\langle r^2 \rangle^{136,124}$ difference in the mean-square nuclear charge radii of the two xenon isotopes. In the present work, $\delta\langle r^2 \rangle^{136,124}$ of $0.276 \pm 0.030 \text{ fm}^2$ was obtained from the weighted average of the Na-like D_1 , Mg-like $3s^2-3s3p$ and Al-like $3s^2 3p-3s^2 3p$ and $3s^2 3p-3s^2 3d$ transitions. This result confirms the value previously determined from the Na-like D_1 transition of $0.269 \pm 0.042 \text{ fm}^2$. The uncertainty of our result is half of that of previous results for the same isotopes obtained from x-ray spectroscopy of muonic atoms, laser spectroscopy of neutral xenon atoms, and a global evaluation of charge radii. Our result is slightly outside the uncertainty of the value obtained from a King plot analysis of comparable precision. The present work illustrates that extreme-ultraviolet spectroscopy of highly charged ions is a viable approach for measurements of charge nuclear radii differences and can be used to benchmark conventional methods.

DOI: [10.1103/PhysRevA.101.062512](https://doi.org/10.1103/PhysRevA.101.062512)

I. INTRODUCTION

Accurate measurements of the charge distributions in nuclei are important for advancing the understanding of nuclear structure, the fundamental forces that hold nucleons together, and the Standard Model. The nuclear charge radius is usually parameterized in terms of the rms radius $\langle r^2 \rangle^{1/2}$ of the nuclear charge distribution. Among the different methods used to measure absolute $\langle r^2 \rangle^{1/2}$ values are muonic-atom spectroscopy [1] and electron scattering [2]. The accuracy of muonic-atom spectroscopy is generally limited by the theoretical treatment of nuclear polarization effects induced by the muon. On the other hand, in electron scattering the difficulty lies in the analysis of the experimental cross sections beyond the first Born approximation. Because of the need for macroscopic amounts of target material, these methods

are typically applied to only stable nuclei, except for at an electron-scattering radioactive isotope facility [3].

In addition to the absolute rms radius values, their variation between different isotopes is also a subject of active research. The most common methods for measuring this parameter are based on the x-ray spectroscopy of inner-shell $K\alpha$ lines [4], optical laser spectroscopy applied to long isotopic chains [5], dielectronic recombination of highly charged few-electron ions [6], and x-ray spectroscopy of highly charged few-electron ions [7]. The spectroscopic shift determined in these methods is a function of the sum of the contributions from the change in volume of the charge distribution, the field shift (FS), and the change in nuclear mass, the mass shift (MS). The MS arises from nuclear recoil and is composed of the normal mass shift (NMS) and the specific mass shift (SMS). The FS depends on the change in the charge radius $\delta\langle r^2 \rangle$ and an electronic factor unique to the studied transition. The value of $\delta\langle r^2 \rangle$ is typically determined by dividing the difference of the measured isotope shift and the calculated value of the MS by the electronic factor obtained from theory. The shift method therefore relies on both precise measurements of the spectral shift and accurate atomic-structure calculations.

Optical laser spectroscopy offers high experimental precision and can be applied to long series of stable and unstable isotopes. The complex large-scale atomic-structure

*Present address: TRIUMF, Vancouver, British Columbia, Canada V6T2A3; rsilwal@triumf.ca

†Present address: Honeywell Quantum Solutions, Broomfield, Colorado 80021, USA.

‡Present address: I. Physikalisches Institut, Justus-Liebig-Universität Gießen, 35392 Giessen, Germany.

calculations of singly ionized and neutral systems, however, can contribute to large overall uncertainties in the extracted charge radii. These calculations are sometimes benchmarked by other methods such as $K\alpha$ measurements and King plot analyses. Spectroscopy of highly charged ions with a few electrons outside closed shells, on the other hand, exploits the simplified electronic structure of such ions for accurate atomic-structure calculations. Due to the strong overlap of the electron-orbital wave functions and the nucleus, the radiative transitions in highly charged ions have an enhanced sensitivity to the charge distribution, making them good nuclear probes. Producing quasi-few-electron ions in large quantities in order to achieve high counting statistics of the emitted spectral lines can pose an experimental challenge.

In our recent publication [8], a method was presented to measure the difference in the mean-square nuclear charge radii of stable isotopes using highly charged Na-like ions confined in an ion trap. The $3s-3p$ transitions in the extreme-ultraviolet (EUV) spectral range were measured and combined with precise atomic structure calculations of the transition wavelength. The method was tested to determine the change in the nuclear charge radius between the (stable) xenon ^{136}Xe and ^{124}Xe isotopes [8]. The method arguably can also be applied to short-lived radioactive isotopes and can complement optical laser spectroscopy to benchmark the atomic-structure calculations involved in these measurements. The choice of Na-like ions was motivated by the accurate theory offered by their simplified electronic structure (quasihydrogenic), the relative ease of producing such ions (in comparison with ions having only a few electrons), their emission in the EUV spectral range, and their high sensitivity to nuclear size.

In highly charged high- Z ions (where Z is the atomic number), *ab initio* atomic structure calculations can provide precise theoretical results for systems with a few electrons outside closed shells. In these systems, the MS effects are generally suppressed, while the FS effects are amplified and can be calculated to high precision. Good examples are Na-like, Mg-like, and Al-like ions with one to three electrons, respectively, outside the Ne-like core. These ions can be produced in abundance in an electron-beam ion trap (EBIT) or electron-beam ion source charge breeder at rare-isotope facilities offering experimental advantages for nuclear radii determinations. The $3s-3p$ transitions in these systems produce strong isolated spectral lines that can be observed with high counting statistics and hence can be measured with high precision by an EUV spectrometer.

Based on the success of our previous determination of the nuclear radius difference between ^{136}Xe and ^{124}Xe isotopes using the Na-like D_1 transitions [8], we extended our studies of $\delta\langle r^2 \rangle^{136,124}$ to the isotope shifts of the Mg-like $3s^2\ ^1S_0-3s3p\ ^1P_1$, Mg-like $3s^2\ ^1S_0-3s3p\ ^3P_1$, Al-like $3s^23p\ ^2P_{1/2}-3s^23p\ ^2P_{3/2}$, and Al-like $3s^23p\ ^2P_{1/2}-3s^23d\ ^2D_{3/2}$ transitions. We present accurate calculations from two different methods: multiconfiguration Dirac-Hartree-Fock (MCDHF) using the GRASP2K package [9] and relativistic many-body perturbation theory (RMBPT) [10,11]. We assess the experimental and theoretical uncertainties of these transitions and determine $\delta\langle r^2 \rangle^{136,124}$ from the combination of the isotope shift data.

We show that the xenon $\delta\langle r^2 \rangle^{136,124}$ nuclear radii difference, obtained from the Mg-like $3s^2-3s3p$ and Al-like $3s^23p-3s^23p$ and $3s^23p-3s^23d$ transitions in addition to the Na-like D_1 transitions, can provide a combined uncertainty smaller than previous measurements. As discussed in Sec. IV, however, our detailed investigation shows that the Na-like D_2 transitions are not suitable for the determination of the $\delta\langle r^2 \rangle^{136,124}$ parameter in xenon.

II. THEORY

For an atomic transition k of transition frequency ν_k , the isotope shift in transition frequency between isotopes A and A' is given by

$$\delta\nu_k^{A,A'} = \delta\nu_{k,MS}^{A,A'} + \delta\nu_{k,FS}^{A,A'}. \quad (1)$$

Here, $\delta\nu_{k,MS}^{A,A'}$ is the MS, and $\delta\nu_{k,FS}^{A,A'}$ is the FS. The MS can be expressed as the change in the expectation value of the relativistic recoil Hamiltonian H_{RMS} of the lower and upper states involved in the atomic transition k :

$$\delta\nu_{k,MS}^{A,A'} = \frac{M' - M}{MM'} \Delta \left[\frac{M}{h} \langle \psi | H_{RMS} | \psi \rangle \right]. \quad (2)$$

Within the $(\alpha Z)^4 m^2/M$ approximation (where m and M are the masses of the electron and the nucleus, respectively), the recoil Hamiltonian for the NMS and the SMS are, respectively, given by the following equations [12–15]:

$$H_{RNMS} = \frac{1}{2M} \sum_i \left[p_i^2 - \frac{Z\alpha}{r_i} \left(\boldsymbol{\alpha}_i + \frac{(\boldsymbol{\alpha}_i \cdot \mathbf{r}_i) \mathbf{r}_i}{r_i^2} \right) \cdot \mathbf{p}_i \right], \quad (3)$$

$$H_{RSMS} = \frac{1}{2M} \sum_{i \neq j} \left[\mathbf{p}_i \cdot \mathbf{p}_j - \frac{Z\alpha}{r_i} \left(\boldsymbol{\alpha}_i + \frac{(\boldsymbol{\alpha}_i \cdot \mathbf{r}_i) \mathbf{r}_i}{r_i^2} \right) \cdot \mathbf{p}_j \right]. \quad (4)$$

Here, M, M' are the nuclear masses for the isotopes A and A' , $\mathbf{r}_i, \mathbf{r}_j$ and $\mathbf{p}_i, \mathbf{p}_j$ are the position and momentum operators for i th and j th electrons, α is the fine-structure constant, and $\boldsymbol{\alpha}_i$ are the 4×4 Dirac matrices. The FS can be expressed in the form of

$$\delta\nu_{k,FS}^{A,A'} = F_k S^{A,A'}, \quad (5)$$

where the electronic parameter F_k is proportional to the change in the electronic density at the origin between the lower and upper states involved in transition k for a given isotope:

$$F_k = \frac{Z}{3\hbar} \left(\frac{e^2}{4\pi\epsilon_0} \right) \Delta |\psi(0)^2|. \quad (6)$$

The Seltzer moment [16] $S^{A,A'}$ is a nuclear parameter that depends on the difference in the nuclear charge distributions of the isotopes under investigation and is given by

$$S^{A,A'} = \delta\langle r^2 \rangle^{A,A'} + \frac{C_2}{C_1} \delta\langle r^4 \rangle^{A,A'} + \frac{C_3}{C_1} \delta\langle r^6 \rangle^{A,A'} + \dots, \quad (7)$$

where $\delta\langle r^2 \rangle^{A,A'}$ is the change in mean-square radii of isotopes A and A' and the C_n 's are the Seltzer coefficients. For light elements, the FS can generally be approximated as

$$\delta\nu_{k,FS}^{A,A'} \approx F_k \delta\langle r^2 \rangle^{A,A'}. \quad (8)$$

TABLE I. The MS and FS coefficients (Coeffs.) and their uncertainties for the Mg-like $3s^2 \ ^1S_0-3s3p \ ^1P_1$ and $3s^2 \ ^1S_0-3s3p \ ^3P_1$ transitions.

Mg-like transition	Theory						Expt.	
	Coeffs.	RMBPT		GRASP2K		$\delta\lambda$ (fm)	$\Delta\delta\lambda$ (fm)	
		$\delta\lambda$ (fm)	$\Delta\delta\lambda$ (fm)	$\delta\lambda$ (fm)	$\Delta\delta\lambda$ (fm)			
$3s^2 \ ^1S_0-3s3p \ ^1P_1$	NMS	-2.34		-2.27				
	SMS	-15.38		-15.29				
	Total MS	-17.72	0.89	-17.56	0.88			
	FS			38.46	0.77			
	FS (HNM)	37.28	0.75	37.02				
	Total	19.56	1.16	19.47	1.17	31.0	15.1	
$3s^2 \ ^1S_0-3s3p \ ^3P_1$	NMS	-4.98		-5.34				
	SMS	-67.58		-65.94				
	Total MS	-72.56	3.63	-71.28	3.56			
	FS			158.01	3.16			
	FS (HNM)	153.38	3.07	152.57				
	Total	80.82	4.75	81.29	4.76	69.8	23.3	

For heavier nuclei, however, the higher-order nuclear moments ($\delta\langle r^4 \rangle$, $\delta\langle r^6 \rangle$, ...) in Eq. (7) can significantly contribute to the FS. The FS can also be calculated directly from the difference in transition energies obtained separately for each isotope A and A' using a specific nuclear charge distribution. However, this requires the calculation of the wave function for each isotope, which sometimes leads to excessive computational work. The difference in the FS obtained from the electronic parameter F_k and the one obtained from the difference in transition energies gives an estimate of contributions of higher-order nuclear moments.

The calculations of the FS and MS coefficients for the Na-like, Mg-like, and Al-like transitions were performed with two methods: RMBPT [10,11] and the MCDHF approach with the GRASP2K package [9]. Both methods have been described in our previous publication [8], but the discussion was in the context of the Na-like D_1 transition. The details of the two methods for the Na-like, Mg-like, and Al-like ions are provided below.

The GRASP2K code was utilized to obtain the atomic state function (ASF) within the MCDHF approach. In this approach, an N -electron atomic state function $\Psi(1, 2, \dots, N)$ can be written as a linear combination of configuration state functions (CSFs) $\Phi(1, 2, \dots, N)$:

$$\Psi(1, 2, \dots, N) = \sum_{i=1}^{N_{CSF}} c_i \Phi(1, 2, \dots, N). \quad (9)$$

Here, N_{CSF} is the number of CSFs used to represent the atomic wave function. Only the CSFs with same parity and total angular momentum J contribute to the ASF. A CSF can be built from the antisymmetric sums of products of N one-electron Dirac spinors known as the Slater determinants. The mixing coefficients c_i 's are obtained by diagonalizing the Hamiltonian using the self-consistent field method. The relativistic configuration interaction (RCI) module was used in the GRASP2K package to consider the Breit interactions and leading QED contributions perturbatively. As emphasized in previous studies [17–19], the finite nuclear distribution

provides a realistic FS in the relativistic approach, and a two-parameter (c , a) Fermi model was therefore assumed to obtain the nuclear potential experienced by the electrons. The ASF for a single-configuration Dirac-Fock solution was calculated for the ^{136}Xe isotope. To consider the correlation effects, the CSF space was expanded by means of single and double excitations from the occupied orbitals to active sets up to $n = 6$ or 7 with orbital quantum number $l_{\max} = 5$ and triple excitations within $n = 3$. These calculations were carried out by adding the virtual orbitals layer by layer. The Breit interactions and the leading QED effects up to $n = 4$ or 5 were also included during the RCI calculations. After obtaining the wave function, the relativistic isotope shift (RIS3) module [20] was used to calculate the MS and the FS. The results are included in Tables I and II as ‘‘GRASP2K.’’ The convergence of the energy, the MS, and the FS quantities was checked, and the agreement of oscillator strengths in the Babushkin and Coulomb gauges was monitored with the addition of each subsequent layer. The convergence of the total MS and FS was within 1%.

As mentioned earlier, the FS was also calculated explicitly by the direct subtraction of the transition energies calculated for each isotope (^{124}Xe and ^{136}Xe) by solving the MCDHF and Breit equations separately. The corresponding values represent the shifts with the higher nuclear moments (HNM) included and are termed ‘‘FS HNM’’ in Tables I and II. Differences of approximately 4% and 11% were observed between the FS coefficient values calculated with and without including the higher moments for the $3s-3p$ transitions and the $3p-3d$ transitions, respectively. The higher nuclear moments vanish for the transition involving the identical overlapping orbitals for the $3p_{1/2}-3p_{3/2}$ transition. This may be due to the cancellation of higher nuclear moment $\delta\langle r^4 \rangle$, $\delta\langle r^6 \rangle$, ... terms for the $3p_{1/2}-3p_{3/2}$ transition, resulting in a nearly zero effect of higher nuclear moments on the FS coefficient.

The RMBPT calculations were performed up to third order [10,11] for the Na-like D_1 transition and the Al-like transitions and up to second order [21] for the Mg-like transitions. Both the Coulomb and Breit interactions were

TABLE II. The MS and FS coefficients (Coeff.) and their uncertainties for the Al-like $3s^23p\ ^2P_{1/2}-3s^23p\ ^2P_{3/2}$ and $3s^23p\ ^2P_{1/2}-3s^23d\ ^2D_{3/2}$ transitions.

Al-like transition	Coeff.	Theory				Expt.	
		RMBPT		GRASP2K		$\delta\lambda$ (fm)	$\Delta\delta\lambda$ (fm)
		$\delta\lambda$ (fm)	$\Delta\delta\lambda$ (fm)	$\delta\lambda$ (fm)	$\Delta\delta\lambda$ (fm)		
$3s^23p\ ^2P_{1/2}-3s^23p\ ^2P_{3/2}$	NMS	-5.09		-5.09			
	SMS	-1.87		-2.51			
	Total MS	-6.96		-7.60	0.38		
	FS			7.36	0.15		
	FS (HNM)	6.94		7.36			
	Total	0.02	0.31	-0.24	0.41	32.1	40
$3s^23p\ ^2P_{1/2}-3s^23d\ ^2D_{3/2}$	NMS			-1.93			
	SMS			-4.60			
	Total MS			-6.53	0.33		
	FS			5.29	0.11		
	FS (HNM)			4.61			
	Total			-1.92	0.34	1.7	27.7

included in each order. To calculate the FS coefficient, the transition energy $\delta\nu_A$ was determined assuming two different nuclear charge distributions, one for each isotope, and forming the difference $\delta\nu_{FS} = \delta\nu_{136} - \delta\nu_{124}$ in each order of RMBPT (testing the results carefully for numerical significance). The RMBPT calculations for the FS converged rapidly, and the third-order contributions to the D_1 and D_2 transitions were less than 0.1% of the total $\delta\nu_{FS}$. Further corrections from QED (self-energy and vacuum polarization) were estimated phenomenologically using the GRASP2K package and were also found to enter at the 0.1% level. The field-shift coefficient was obtained from

$$F_k = \frac{\delta\nu_{FS}}{\delta\langle r^2 \rangle}, \quad (10)$$

where $\delta\langle r^2 \rangle$ is the change in mean-square radii of the two nuclear charge distributions assumed in the calculation.

The whole procedure was repeated for several pairs of nuclear charge distributions, involving changes in charge density in both the surface and volume regions of the nucleus, and F_k was found to fluctuate at the 1% to 2% level. This was taken to indicate the likely level of nuclear-model dependence. The dominant uncertainty in the FS coefficient is attributed to this parametrization uncertainty (nuclear-distribution model-dependence uncertainty), which is on the order of 1% and is due to the basic assumption that the FS is proportional to $\delta\langle r^2 \rangle$ rather than the more correct Seltzer moment $S^{A,A'}$ given in Eq. (7). The uncertainty due to the third-order correlation effects as well as the QED corrections (self-energy and vacuum polarization) was found to be of the order of 1% or less, which is also the level of the discrepancy between the RMBPT and GRASP2K results in Tables I and II. The dominant uncertainty in the MS calculation is due to omitted higher-order relativistic corrections in the nuclear-recoil formalism. At present, using the operators in Eqs. (3) and (4), we include relativistic corrections up to order $(Z\alpha)^4(m/M)mc^2$, that is, to order $(Z\alpha)^2$ relative to the lowest-order nonrelativistic mass shift. The omitted effects start in order $(Z\alpha)^5(m/M)mc^2$, or in order $(Z\alpha)^3$ relative to the lowest-order mass shift. A crude

first estimate of these omitted corrections can be made by evaluating $(Z\alpha)^3$, which results in the reported 5% value. The nuclear-recoil terms of this order and higher have been evaluated numerically for H-like ions [22]. By scaling the H-like data in Ref. [22], we estimate that in Na-like Xe the omitted one-electron nuclear-recoil terms in relative order $(Z\alpha)^3$ are indeed of order the of 5% of the mass shift for a $3s-3p$ transition. This gives only an order-of-magnitude estimate of the true effect, however, because in many-electron ions additional two-electron terms (analogous to the specific mass shift) are also present in relative order $(Z\alpha)^3$, and to our knowledge these have not been treated fully. At present, the estimated 5% error in the mass shift is smaller than the experimental error, and this issue is not critical, although it could become important in future, more precise measurements.

III. EXPERIMENT

Highly charged Xe ions of the two isotopes, ^{136}Xe and ^{124}Xe , were produced and trapped in the EBIT at the National Institute of Standards and Technology (NIST) by first separately injecting the purified isotopes as gases into the injection system [23] at a pressure of 2×10^{-3} Pa. They were then injected into the EBIT and ionized to the charge state of interest via electron impact ionization. An electron beam current of 150 mA with an energy of 6 keV was used during the entire series of measurements. The beam energy was set by a potential difference between the drift tube assembly floated at 6 kV and the electron gun, which was held at the ground potential. Electrostatic potentials of 260, 0, and 500 V were applied to the upper, center, and lower drift tube electrodes with respect to the assembly, respectively, for trapping the Xe ions in the axial direction. The ions were radially confined by the space-charge potential of the electron beam compressed by the 2.7-T field of the superconducting magnet. At these settings, the Na-like Xe^{43+} and nearby charge-state ions were the most abundant charge states observed in the trap.

From theoretical estimates, the isotope shifts of the $3s-3p$ transitions in Na-like and Mg-like ions between the two

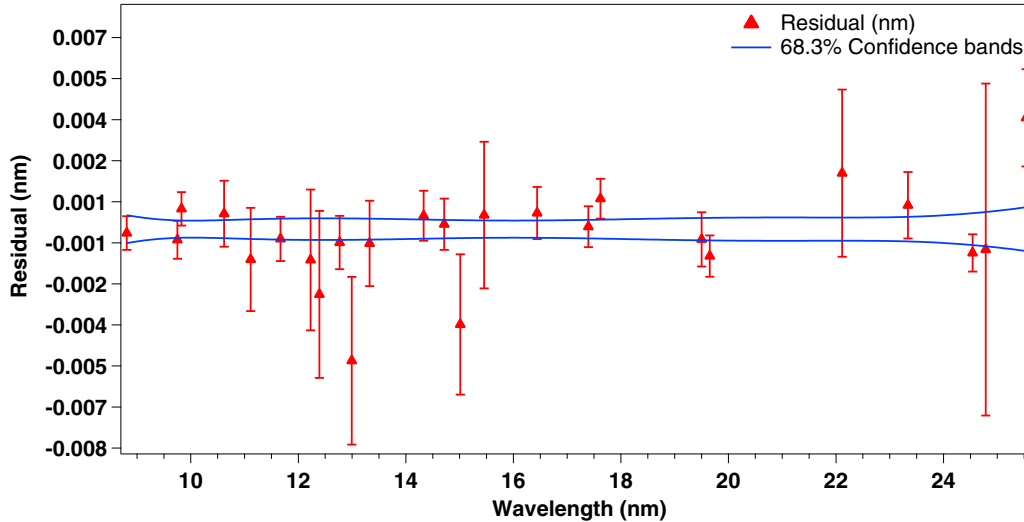


FIG. 1. Residual of the calibration points with their associated uncertainties shown as error bars (red). The 68.3% confidence bands are shown in blue.

isotopes ^{136}Xe and ^{124}Xe are less than 10^{-4} nm, and the Al-like transitions are an additional factor of 2 or 3 smaller. In order to observe such a small shift, high counting statistics from over 600 EUV spectra, including background spectra for calibrations, had to be collected for 300 s each using a flat-field grazing incidence EUV spectrometer [8,24]. Each 300-s spectra contained five 60-s frames that provided input for a cosmic-ray filter algorithm [25]. A constant background of the readout noise was also subtracted from the spectra. A total of 400 spectra were analyzed in this study after excluding the “background spectra,” which were taken with no ions in the trap and statistical outliers. Roughly hour-long series of spectra were taken for each isotope before switching to the other. Each of these series consisted of ten to twelve 300-s data accumulation periods. The switch between the two isotopes was synchronized with the automatic liquid-nitrogen refill of a container providing cooling to the collector of the EBIT.

The dispersion function to convert the pixel number to wavelength was determined by a standard calibration procedure [25] using well-known EUV spectral lines of Xe, Ne, and Ar [26–28]. Neutral Ne atoms were injected into the EBIT via the gas injection system at an injection pressure of 2×10^{-3} Pa. A strong Ar line at 22.115(3) nm was observed in the Ne spectra when the trap was periodically emptied to get rid of heavy impurity ions. This line comes from residual Ar remaining in trace amounts in the two ion pumps of the EUV spectrometer. Lines of accumulated Ba impurities originating from the electron-gun cathode coated with BaO_2 were also observed in the spectra when the trap was not emptied. A weighted polynomial function was determined from the calibration lines where the weight was given by the total uncertainties of each calibration line. These uncertainties were determined from the quadrature sum of the uncertainty in the wavelength values adopted from the literature, the fit uncertainty of the calibration peaks, and a constant estimated systematic uncertainty of 0.0006 nm obtained by requiring the reduced χ^2 of the fit to be close to 1. The resulting calibrated spectral region ranged from 7.54 to 26.25 nm with

the calibration polynomial

$$\begin{aligned} \Lambda[\text{nm}] = & 7.5403(12) + 6.7535(6) \times 10^{-3}x \\ & + 1.2536(6) \times 10^{-6}x^2 - 4.2522(1740) \times 10^{-11}x^3. \end{aligned} \quad (11)$$

Here, x is the pixel number. The residual of the calibration data points with the corresponding uncertainty is shown in Fig. 1. This residual shows that the overall uncertainty of the polynomial fit is within ± 0.002 nm (68.3% confidence level).

Figure 2 shows typical spectra for both isotopes taken over the spectral region that includes the Na-like, Mg-like, and Al-like transitions. The wavelength range covered by the grating of the spectrometer allowed for the simultaneous measurement of different diffraction orders of the same transitions in a single spectrum. Consequently, the first and second orders of the Na-like D_1 transition [12.3935(9) nm] and the Mg-like $3s^2 \ ^1S_0$ - $3s3p \ ^3P_1$ transition [12.9968(7) nm] were observed. Similarly, the second and third orders of the Na-like D_2 transition [6.6622(4) nm], the Mg-like $3s^2 \ ^1S_0$ - $3s3p \ ^1P_1$ transition [6.2920(3) nm], and the Al-like $3s^23p \ ^2P_{1/2}$ - $3s^23d \ ^2D_{3/2}$ transition [5.2159(3) nm] were simultaneously measured in every collected spectrum. The third-order Al-like transition was blended with the first-order P-like $3p^3 \ ^2P_{3/2}$ - $3p^3 \ ^2D_{5/2}$ transition at 15.6447(25) nm [26]. Only the first order of the Al-like $3s^23p \ ^2P_{1/2}$ - $3s^23p \ ^2P_{3/2}$ transition [15.0141(9) nm] was observed since the second-order spectra were just outside the studied spectral range. The accessibility of multiple orders of a spectral line reduces the overall uncertainties by randomizing line blends and increasing the counting statistics.

The process for determining the isotope shift of each line involved several steps. Briefly, the spectra were first analyzed by finding the centroid of each line. The centroid (in pixel numbers) was then plotted as a function of measurement number for each isotope, and the data were fit to a polynomial to remove time-dependent variations in the data. The isotopic

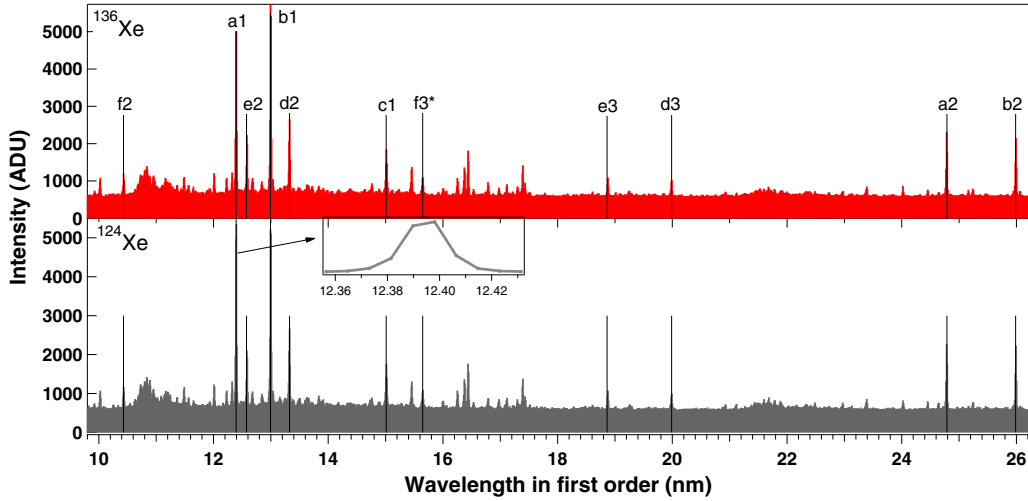


FIG. 2. Xenon spectra for isotopes 136 (top, in red) and 124 (bottom, in gray). Lines labeled a1, a2, b1, and b2 correspond to the first and second orders of the Na-like $3s^2\ ^2S_{1/2}-3p^2\ ^2P_{1/2}$ (D_1) and Mg-like $3s^2\ ^1S_0-3s3p^3\ ^3P_1$ transitions, respectively. Line c1 represents the first order Al-like $3s^23p^2\ ^2P_{1/2}-3s^23p^2\ ^2P_{3/2}$ transition. Similarly, d2, d3, e2, e3, f2, and f3 correspond to the second and third orders of the Na-like $3s^2\ ^2S_{1/2}-3p^2\ ^2P_{3/2}$ (D_2), Mg-like $3s^2\ ^1S_0-3s3p^3\ ^1P_1$, and Al-like $3s^23p^2\ ^2P_{1/2}-3s^23d^2\ ^2D_{3/2}$ transitions, respectively. The asterisk (*) following f3 represents a blend with a P-like $3p^3\ ^2P_{3/2}-3p^3\ ^2D_{5/2}$ transition at 15.6447(25) nm. A zoomed-in view of the first-order Na-like D_1 peak is also given in the inset.

shift was then found from these fits. The spectral shift in pixel number was converted to a spectral shift in wavelength, and this was used to determine the change in the nuclear charge radius. We now present the details of the analysis below.

First, the pixel number corresponding to the line centroid of the peaks for the Na-like, Mg-like, and Al-like Xe transitions

was determined using the weighted average center-of-mass method given by

$$x_{cm} = \frac{\sum_i x_i I_i}{\sum_i I_i}, \quad (12)$$

where x_i is the i th pixel with line intensity I_i . This method was chosen to evaluate the centroid position instead of a

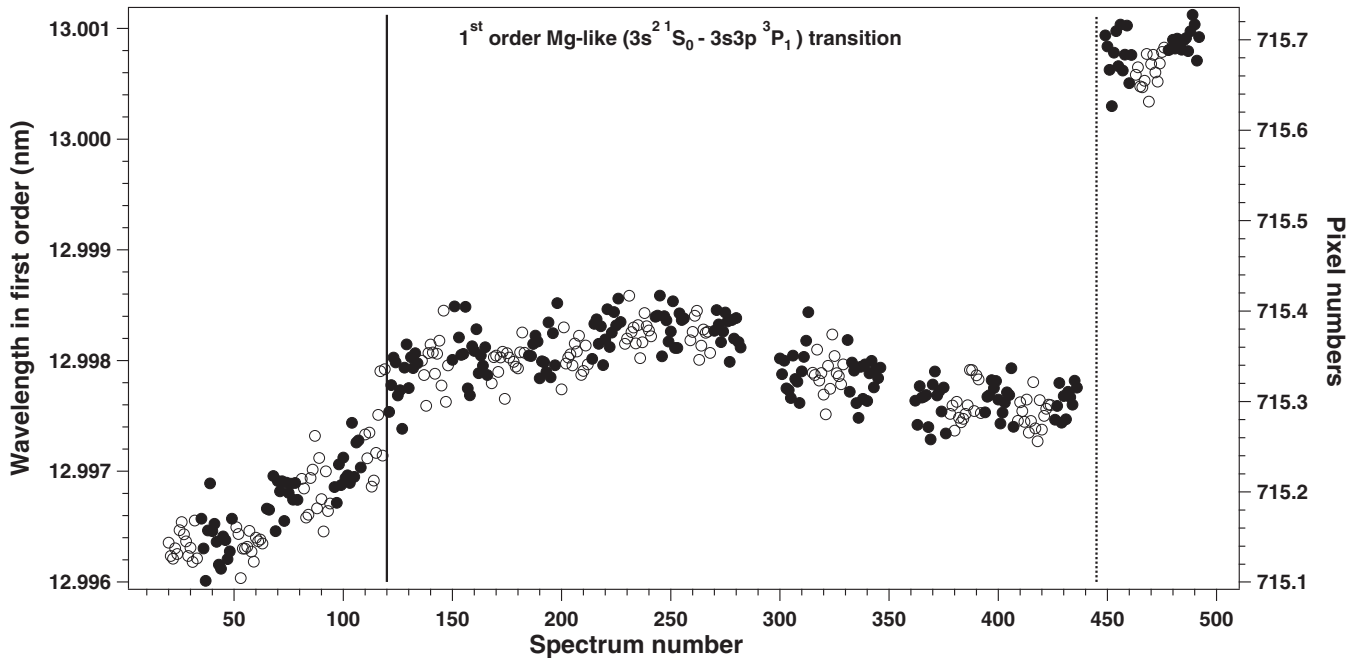


FIG. 3. Scatterplot of the centroid position of the first-order Mg-like $3s^2\ ^1S_0-3s3p^3\ ^3P_1$ transition in units of nanometers (left) and pixel numbers (right) as a function of the spectrum number for the 136 (solid circle) and 124 (open circles) isotopes. The solid and dashed lines at measurement numbers 120 and 445 indicate a change in experimental conditions (see text). These regions were fit separately during the analysis.

peak-fitting function to avoid line-shape model-dependent uncertainties. As discussed more below, different numbers of pixels around the peaks were chosen to estimate their centroid positions, and the isotope-shift results were systematically analyzed to check the consistency of the result. We found that seven pixels around the mean of the centroid positions best represented the peaks, and this was used to calculate the centroids for the analysis.

The distribution of the line-centroid positions was evaluated to investigate any time-dependent systematic drifts during the 4-day data-taking period. Figure 3 shows the line-centroid positions in pixel numbers and also in units of wavelength using the conversion given in Eq. (11) as a function of the spectrum number for the Mg-like $3s^2 \ ^1S_0\text{-}3s3p \ ^3P_1$ transition in the first order. Clear signs of time-dependent drifts and shifts in the line centroid were observed. These changes were especially apparent at measurement numbers 120 and 445, as shown in Fig. 3. The first shift, shown by the solid line at measurement number 120, was caused by the addition of liquid nitrogen to the CCD dewar of the EUV spectrometer. The large shift, shown in Fig. 3 by the dashed line at measurement number 445, was caused by a combination of the addition of liquid nitrogen to the EUV CCD dewar and the replacement of the liquid-helium dewar used to cool the superconducting magnet of the EBIT. The slow drift in the line-centroid position is believed to be the result of temperature-dependent effects in the CCD chip as well as the EBIT plasma (e.g., changes in the electron-beam position). It must be noted that the scale of these drifts is within the uncertainties of the reported absolute wavelength positions.

To properly treat the systematic drifts for the evaluation, the time-ordered sequence of the line-centroid pixel numbers was divided into three regions separated by the two positions with significant shifts (measurement numbers 120 and 445). Third-order polynomials were used to fit the long-term variation of the line-centroid positions with different polynomial coefficients for the three regions. The same polynomial functions were used for ^{136}Xe and ^{124}Xe except for a constant

parameter (a constant offset) added to the polynomial function to extract the isotope shift. The residuals obtained from the fits were binned to determine their statistical distribution as a check of the analysis procedure. The Gaussian fits of the residuals for the two distributions agreed to within the shift uncertainty. As an example, the fit to a partial series of the time-ordered distribution of the line-centroid positions of the Mg-like $3s^2 \ ^1S_0\text{-}3s3p \ ^3P_1$ transition in first and second orders and the residuals from the fits are shown in Figs. 4 and 5. Different bin sizes were chosen to obtain the difference in the centroids of the Gaussian fits of the residual distributions, and no systematic dependence of the result on the bin sizes was observed.

Several systematic tests were performed as a test of the obtained results. As previously discussed, the spectra were analyzed by choosing different numbers of pixels under the spectral lines when determining their centroid positions. Different polynomial orders were used to fit the time-ordered distributions of the centroid positions, and a systematic study of the result with these values was conducted. Figures 6 and 7 show that when the number of pixels under the peaks and the order of the polynomial fits were varied, the isotope shifts of the Na-like D_1 and Mg-like $3s^2 \ ^1S_0\text{-}3s3p \ ^3P_1$ transitions in first order agreed within their uncertainties. Similar studies of the residual distribution with varying bin sizes were performed. In all the reported values, the difference in the Gaussian centroid of the binned residual was an order of magnitude smaller than the uncertainty of the measured shift.

The isotope shift in units of pixel number ($\delta x[\text{pno.}]$) was approximately converted into a shift in units of wavelength ($\delta \Lambda[\text{nm}]$) by multiplying the shift with the transition wavelength ($\Lambda[\text{nm}]$) as found using the dispersion function Eq. (11):

$$\delta \Lambda[\text{nm}] = \delta x[\text{pno.}] \times \Lambda[\text{nm}]. \quad (13)$$

The uncertainty in the wavelength value of the isotope shift $\Delta(\delta \Lambda[\text{nm}])$ is given by

$$\Delta(\delta \Lambda[\text{nm}]) = \sqrt{(\Delta \delta x[\text{pno.}])^2 \times (\Lambda[\text{nm}])^2 + (\Delta \Lambda[\text{nm}])^2 \times (\delta x[\text{pno.}])^2}, \quad (14)$$

where $\Delta \Lambda[\text{nm}]$ is the uncertainty in the dispersion function at the position of the line and $\Delta(\delta x[\text{pno.}])$ is the uncertainty in the isotope shift in units of pixel number. The difference in nuclear charge radius between ^{124}Xe and ^{136}Xe , $\delta \langle r^2 \rangle^{136,124}$, was evaluated by a procedure explained in detail in the following section.

IV. RESULTS AND DISCUSSION

Table III lists the measured isotope shifts and the difference in the mean-square radii $\delta \langle r^2 \rangle^{136,124}$ along with their uncertainties for the Na-like $3s \ ^2S_{1/2}\text{-}3p \ ^2P_{1/2}$ transition, Mg-like $3s^2 \ ^1S_0\text{-}3s3p \ ^3P_1$ and $3s^2 \ ^1S_0\text{-}3s3p \ ^1P_1$ transitions, and the Al-like $3s^2 3p \ ^2P_{1/2}\text{-}3s^2 3d \ ^2D_{3/2}$ and $3s^2 3p \ ^2P_{1/2}\text{-}3s^2 3p \ ^2P_{3/2}$ transitions. The centroid positions of the second order of the

Na-like D_1 transition, the Mg-like $3s^2 \ ^1S_0\text{-}3s3p \ ^3P_1$ transition, and the third order of the Mg-like $3s^2 \ ^1S_0\text{-}3s3p \ ^1P_1$ transition all showed systematic dependence on the number of pixels used to determine the centroid, suggesting possible blends with other line features. Hence, these transitions are not shown in Table III and were therefore excluded in the determination of the overall $\delta \langle r^2 \rangle^{136,124}$. Similar to a previous study by Gillaspay [29] that indicated an energy-dependent trend for the Na-like D_2 transition, the centroid position of the this transition in first and second orders showed systematic dependence on the beam energy. This indicates possible blends, and it too was excluded from the analysis. As seen in Table III, the measured shifts of the Al-like $3s^2 3p \ ^2P_{1/2}\text{-}3s^2 3d \ ^2D_{3/2}$ and $3s^2 3p \ ^2P_{1/2}\text{-}3s^2 3p \ ^2P_{3/2}$ transitions are smaller than the experimental uncertainty. Our overall measurement uncertainty

TABLE III. The experimental shifts (^{136}Xe - ^{124}Xe) and the difference in the mean-square radii $\delta\langle r^2 \rangle^{136,124}$ with their associated uncertainties for different orders of the Na-like $3s$ - $3p$, Mg-like $3s^2$ - $3s3p$ transitions, and Al-like $3s^23p$ - $3s^23p$ and $3s^23p$ - $3s^23d$ transitions.

Transitions	Order	Shift (fm)	Uncertainty (fm)	$\delta\langle r^2 \rangle^{136,124}$ (fm ²)	$\Delta\delta\langle r^2 \rangle$ (fm ²)
Na-like ($3s^2\ ^1S_0$ - $3p\ ^2P_{1/2}$)	first	65.5	20.6	0.269	0.042
Mg-like ($3s^2\ ^1S_0$ - $3s3p\ ^3P_1$)	first	69.8	23.3	0.268	0.045
Mg-like ($3s^2\ ^1S_0$ - $3s3p\ ^1P_1$)	second	31.0	15.1	0.379	0.118
Al-like ($3s^23p\ ^2P_{1/2}$ - $3s^23d\ ^2D_{3/2}$)	second	1.7	27.7	0.517	1.740
Al-like ($3s^23p\ ^2P_{1/2}$ - $3s^23p\ ^2P_{3/2}$)	first	32.1	40.0	1.596	1.668

was dominated by time- and temperature-dependent systematic drifts, as discussed above. Furthermore, the predicted shifts for the Al-like transitions are smaller than those of the Na-like and Mg-like transitions due to the weaker penetration of the p and d orbitals near the nucleus, as seen in Table II. Nevertheless, these Al-like transitions were used for the determination of $\delta\langle r^2 \rangle^{136,124}$. We note that our observation of no apparent shift for the Al-like transition is consistent with the theoretical predictions, providing confidence in the data analysis approach used here.

The value of the MS and FS coefficients calculated using both the RMBPT method and the MCDHF method using the GRASP2K package are given in Tables I and II for the Mg-like $3s^2\ ^1S_0$ - $3s3p\ ^1P_1$ and $3s^2\ ^1S_0$ - $3s3p\ ^3P_1$ transitions and the Al-like $3s^23p\ ^2P_{1/2}$ - $3s^23p\ ^2P_{3/2}$ transition, respectively. The coefficients for the Na-like D_1 transition were reported in a previous publication [8]. For the Al-like $3s^23p\ ^2P_{1/2}$ - $3s^23d\ ^2D_{3/2}$ transition, we do not report the calculations from RMBPT. This is due to the fact that, for the $3d_{3/2}$ state, there is a nearly vanishing energy denominator associated

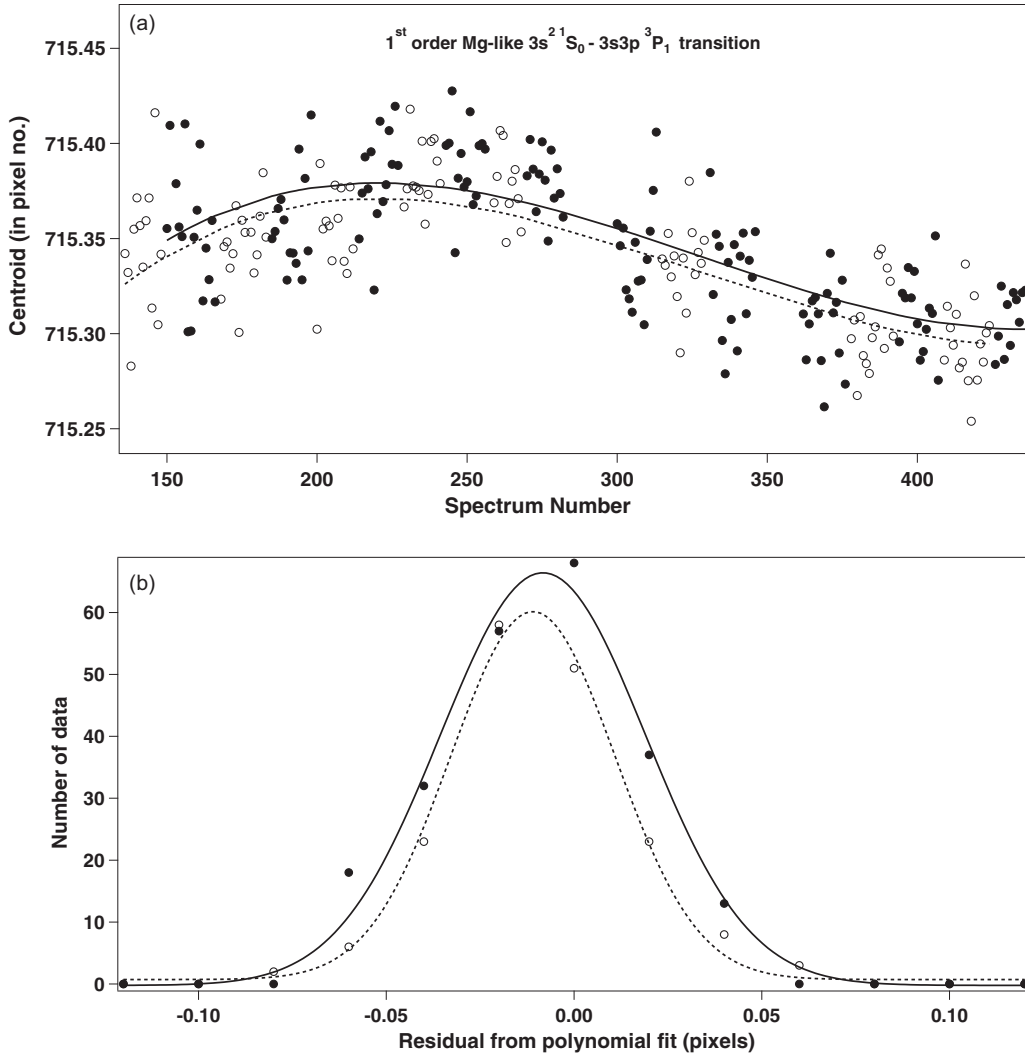


FIG. 4. (a) Polynomial fit (third order) of a partial time-ordered sequence of the centroid position of the first-order Mg-like $3s^2\ ^1S_0$ - $3s3p\ ^3P_1$ transition as a function of spectrum number for the 136 (solid circles) and 124 (open circles) isotopes. (b) The residual of the fits for the two isotopes binned and fitted with a Gaussian distribution.

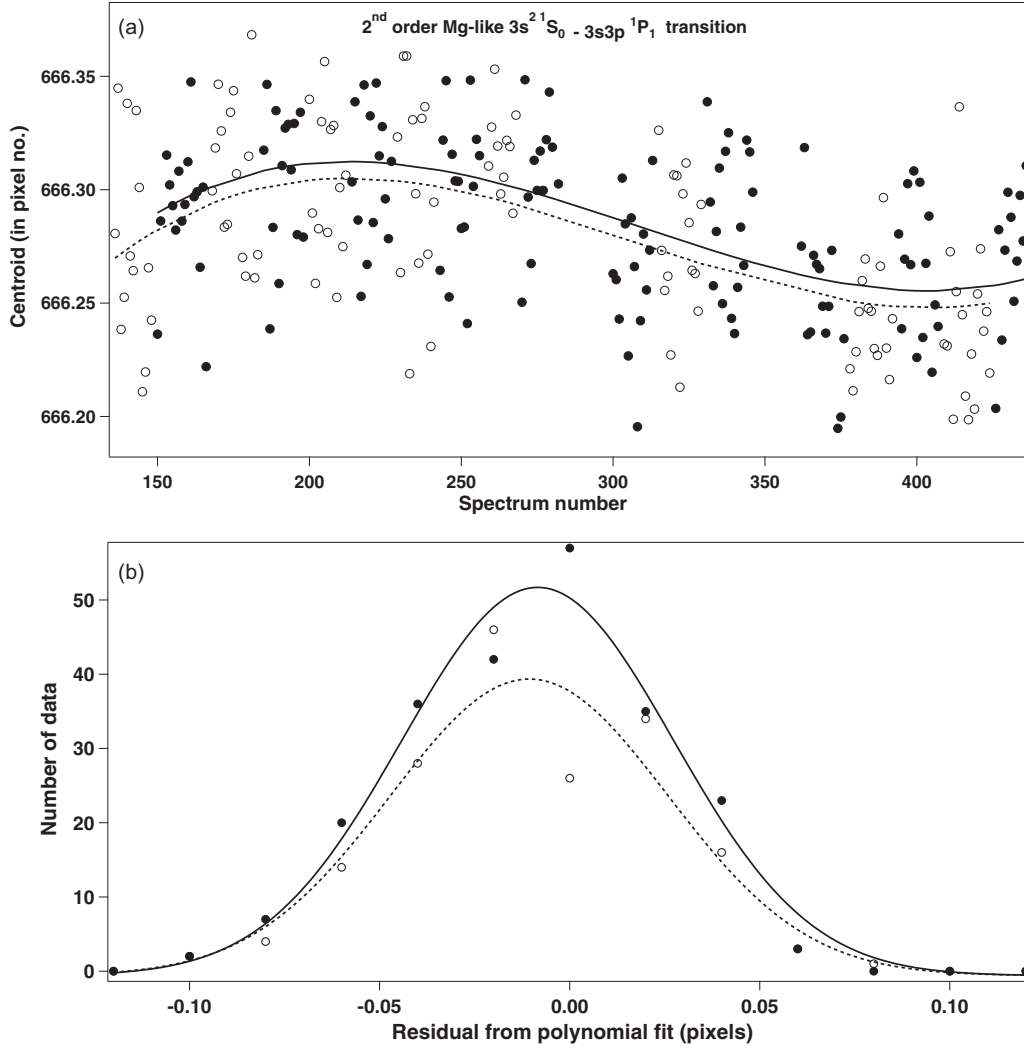


FIG. 5. (a) Polynomial fit (third order) of the partial time-ordered sequence of the centroid position of the second-order Mg-like $3s^2\ ^1S_0 - 3s3p\ ^1P_1$ transition as a function of spectrum number for the 136 (solid circles) and 124 (open circles) isotopes. (b) The residual of the fits for the two isotopes binned and fitted with a Gaussian distribution.

with the $(3s, 3d_{3/2}) \rightarrow 3p^2$ excitation channel destroying the convergence of RMBPT. Also, the coefficients for this transition are dominated by the correlation effects, resulting in inaccurate results with the RMBPT method. The MS and the FS coefficients were calculated in units of terahertz \times atomic mass unit and gigahertz per square femtometer, respectively, but were then converted to units of femtometers by using $1\text{ cm}^{-1} = 299979.2458\text{ MHz}$, $M_{124} = 123.9058942\text{ amu}$, and $M_{136} = 135.907214\text{ amu}$.

In order to achieve an accurate evaluation of $\delta\langle r^2 \rangle^{136,124}$, higher nuclear moments must be included in the calculation of the FS. The contribution of these higher-order terms was approximately 4% for $3s-3p$ transitions. The final uncertainty of $\delta\langle r^2 \rangle^{136,124}$ was found using the equation

$$\Delta\delta\langle r^2 \rangle^{136,124} = \sqrt{\left(\frac{\Delta\delta v_{FS}}{F}\right)^2 + \left(\frac{\Delta F \cdot \delta v_{FS}}{F^2}\right)^2 + (\Delta S_{HO})^2}. \quad (15)$$

Here $\Delta\delta v_{FS}$ was given by the quadrature sum of the experimental uncertainty of the total shift and the theoretical MS uncertainty, $\Delta\delta v_{FS} = \sqrt{(\Delta\delta v_{exp})^2 + (\Delta\delta v_{MS})^2}$, and ΔS_{HO} represented the uncertainty due to the higher-order terms of the relative nuclear charge radii. The total uncertainties in theory propagated to $\approx 4\%$ uncertainty in the value of extracted $\delta\langle r^2 \rangle^{136,124}$. This uncertainty, however, was much smaller than the uncertainty in the measured value.

The differences in the mean-square radii for the different Na-like, Mg-like, and Al-like transitions are listed in Table III. These values resulted in an overall reported average value of

$$\delta\langle r^2 \rangle^{136,124} = 0.276 \pm 0.030\text{ fm}^2. \quad (16)$$

This average result agrees with the measured value of $0.242 \pm 80\text{ fm}^2$ by Borchers *et al.* [30] and with the value of $0.290 \pm 0.069\text{ fm}^2$ reported by Angeli and Marinova [31] in their global evaluation of charge radii. The result is also in agreement with a value of $0.324 \pm 0.057\text{ fm}^2$ obtained through a King plot analysis by Fricke and Heilig [32], but it is slightly outside the value of $0.350 \pm 0.030\text{ fm}^2$ [33] acquired

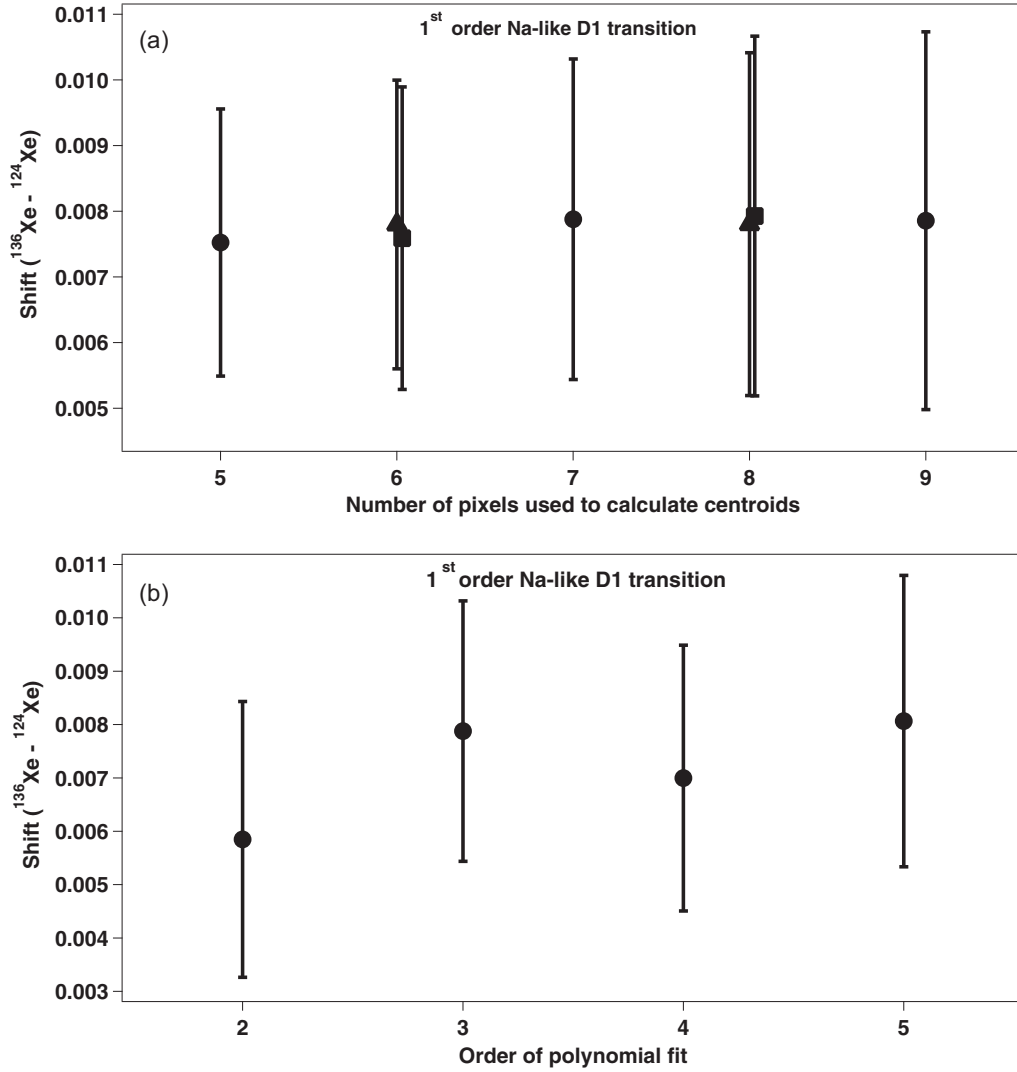


FIG. 6. Isotope shift ($^{136}\text{Xe} - ^{124}\text{Xe}$) in pixel numbers for the first-order Na-like D_1 transition with changing the (a) number of pixels chosen to calculate the line centroid and the associated error bars and (b) polynomial order while fitting the time-ordered distribution of the centroid positions. The squares and the triangles correspond to even pixel numbers with one extra pixel on the left and right, respectively.

from a King plot analysis of optical isotope shifts [30] vs muonic-atom spectroscopy measurements [32]. The comparison of our result with the previous measurement and theory is shown in Fig. 8.

Our new and more accurate result supports our conclusion from our previous work [8]. It can be interpreted as resolving the disagreement between different methods for evaluating F values, providing further support for nuclear models describing particular aspects of the nuclear structure. Libert *et al.* [33] performed nuclear-structure calculations including dynamical deformation of the evolution of the mean-square charge radius of xenon over a long chain of isotopes. They compared their results with the experimental charge radii calculated by combining Borchers *et al.*'s [30] optical isotope shift measurements with F_k obtained from (a) semiempirical atomic-structure calculations and (b) a King plot analysis of muonic-atom spectroscopy data and the results from [30]. Their model including dynamical deformation significantly disagrees with the evolution of charge radii predicted with the F_k value calculated from the King plot analysis. This

disagreement is suggested to be a result of deducing the charge-radius values from the muonic-atom spectroscopy measurements that were obtained for only stable isotopes near the magic neutron number $N = 82$, where the changes in charge radius are small. The King plot analysis may therefore not yield an F_k factor sufficiently accurate for nuclei far from stability. Moreover, the uncertainty of the charge radii obtained by muonic-atom spectroscopy is largely due to the nuclear polarization corrections, and these muonic charge radii were corrected assuming a spherical nuclear shape. The authors hint that this assumption may not be adequate, as deformation already exists for the lightest stable isotopes. Our result provides an independent test of the two methods used to obtain the F_k factors and, incidentally, tests the validity of the corrections and assumptions used to determine the muonic charge radii of stable isotopes. Our result agrees with Libert *et al.*'s model [33] including dynamical deformation and, as such, agrees with the semiempirical F_k value. Our result shows the importance of including dynamical effects in the evolution of charge radii of xenon isotopes.

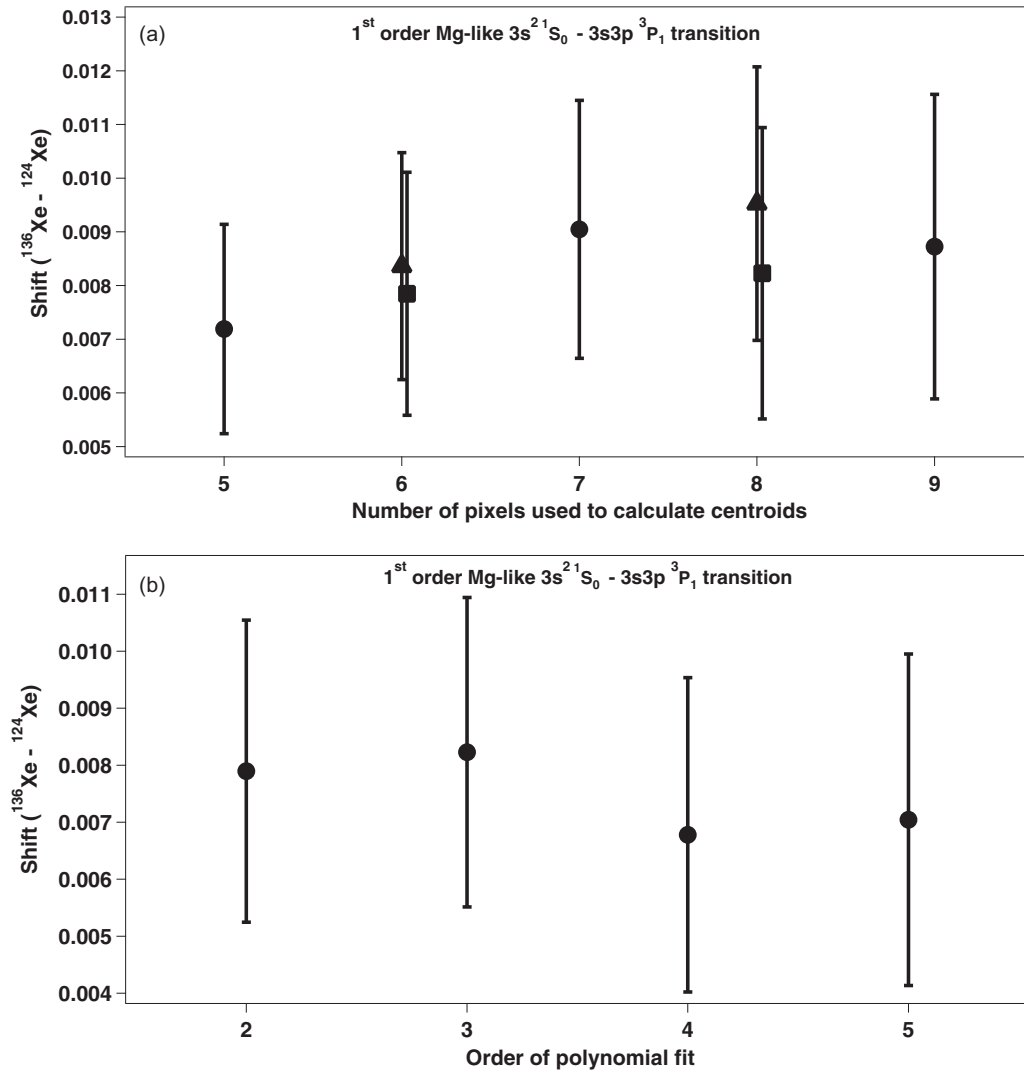


FIG. 7. Isotope shift ($^{136}\text{Xe} - ^{124}\text{Xe}$) in pixel numbers for the first-order Mg-like $3s^2\ ^1S_0 - 3s3p\ ^3P_1$ transition with changing the (a) number of pixels chosen to calculate the line centroid with the associated error bars and (b) polynomial order while fitting the time-ordered distribution of the centroid positions. The squares and the triangles correspond to even pixel numbers with one extra pixel on the left and right, respectively.

The accuracy of theory for Na-like, Mg-like, and Al-like systems, combined with the resolution offered by an EUV grazing-incidence grating spectrometer, allowed us to measure the difference in mean-square nuclear charge radii of xenon isotopes 136 and 124 with an accuracy higher than existing experimental methods. The uncertainty in the measured wavelength shift dominates the overall uncertainty in the determination of the charge-radius difference.

Improvements in the experimental apparatus can potentially reduce the experimental uncertainty. First, by minimizing the amplitude of the time-dependent drifts, the systematic uncertainty can be improved. The precision of the EUV spectrometer can be increased using a higher line density grating for higher resolving power. Higher statistics can be achieved by adding multiple EUV spectrometers on the other radial ports of the EBIT (up to six in the case of our EBIT), and this would also reduce the systematics due to the electron beam drift. One of the challenges during the measurement was the line of interest blending with other features. This

arose due to the existence of lower charge states in the trap created by charge exchange of the charge states of interest with the neutrals. To avoid this effect, an alternative method, such as a pulsed injection technique, could be applied instead of continuous gas injection.

Our method can be used to calibrate theoretical SMS and F_k values used in optical laser spectroscopy measurements of isotope shifts in neutral atoms or singly charged ions. These values are difficult to calculate in multielectron systems, and hence, they are often benchmarked through King plot analyses of muonic-atom spectroscopy data against optical measurements or by comparing two sets of optical measurements against one another. Our method offers another alternative to perform such benchmarking through a direct comparison to optical measurements or by including EUV measurements in King plot analyses. Finally, our method can also be applied to measure changes in nuclear charge radii of rare (radioactive) isotopes of high yields that are either currently available or will soon be available at future facilities [8].

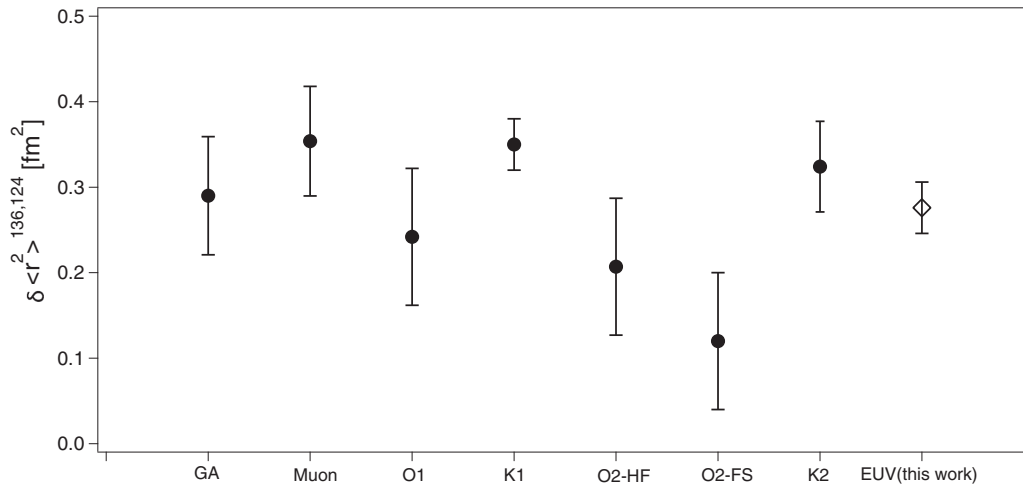


FIG. 8. The change in mean-square nuclear charge radii between the xenon isotopes ^{136}Xe and ^{124}Xe , $\delta \langle r^2 \rangle^{136,124}$, as measured by EUV spectroscopy of the Na-like D_1 , Mg-like $3s^2-3s3p$ and Al-like $3s^23p-3s^23p$ and $3s^23p-3s^23d$ transitions (open diamond) compared with previous measurements and analyses (solid circles). GA: global analysis value by [31]; Muon: muonic-atom spectroscopy [1]; O1: optical shift by laser-spectroscopy [30]; K1: King plot analysis combining the optical measurements with the muonic-atom results [33]; O2-HF and O2-FS: optical (interferometer) shift based on the Hartree-Fock method and Fermi-Segre calculations [34]; K2: King plot analysis by Fricke and Heilig [32]; EUV (this work): result from the work presented here.

ACKNOWLEDGMENTS

This work was partially funded by NIST Grant Award No. 70NANB16H204 of the Measurement Science and Engineering (MSE) Research Grant Programs. A.L. and A.C.C.V. acknowledge support from the National Science Foundation under Grant No. PHY-1565546. J.M.D. acknowledges

funding from the National Research Council Research Associateship Award at NIST. G.G. acknowledges support from NSERC (Canada). We would like to thank D. Takacs for his help with the initial data analysis. Any opinions, findings, and conclusions or recommendations expressed in this material are those of the author(s) and do not necessarily reflect the views of the National Science Foundation.

- [1] G. Fricke, C. Bernhardt, K. Heilig, L. A. Schaller, L. Schellenberg, E. B. Shera, and C. W. DeJager, *At. Data Nucl. Data Tables* **60**, 177 (1995).
- [2] R. Hofstadter, *Rev. Mod. Phys.* **28**, 214 (1956).
- [3] K. Tsukada, A. Enokizono, T. Ohnishi, K. Adachi, T. Fujita, M. Hara, M. Hori, T. Hori, S. Ichikawa, K. Kurita *et al.*, *Phys. Rev. Lett.* **118**, 262501 (2017).
- [4] R. T. Brockmeier, F. Boehm, and E. N. Hatch, *Phys. Rev. Lett.* **15**, 132 (1965).
- [5] P. Campbell, I. D. Moore, and M. R. Pearson, *Prog. Part. Nucl. Phys.* **86**, 127 (2016).
- [6] C. Brandau, C. Kozhuharov, Z. Harman, A. Muller, S. Schippers, Y. S. Kozhedub, D. Bernhardt, S. Bohm, J. Jacobi, E. W. Schmidt *et al.*, *Phys. Rev. Lett.* **100**, 073201 (2008).
- [7] S. R. Elliott, P. Beiersdorfer, M. H. Chen, V. Decaux, and D. A. Knapp, *Phys. Rev. C* **57**, 583 (1998).
- [8] R. Silwal, A. Lapierre, J. D. Gillaspay, J. M. Dreiling, S. A. Blundell, Dipti, A. Borovik, Jr., G. Gwinner, A. C. C. Villari, Yu. Ralchenko, and E. Takacs, *Phys. Rev. A* **98**, 052502 (2018).
- [9] P. Jönsson, G. Gaigalas, J. Bieroń, C. Froese Fischer, and I. P. Grant, *Comput. Phys. Commun.* **184**, 2197 (2013).
- [10] W. R. Johnson, S. A. Blundell, and J. Sapirstein, *Phys. Rev. A* **37**, 2764 (1988).
- [11] W. R. Johnson, S. A. Blundell, and J. Sapirstein, *Phys. Rev. A* **38**, 2699 (1988).
- [12] C. W. P. Palmer, *J. Phys. B* **20**, 5987 (1987).
- [13] V. M. Shabaev and A. N. Artemyev, *J. Phys. B* **27**, 1307 (1994).
- [14] V. M. Shabaev, *Phys. Rev. A* **57**, 59 (1998).
- [15] E. Gaidamauskas, C. Nazé, P. Rynkun, G. Gaigalas, P. Jönsson, and M. Godefroid, *J. Phys. B* **44**, 175003 (2011).
- [16] E. C. Seltzer, *Phys. Rev.* **188**, 1916 (1969).
- [17] S. A. Blundell, P. E. G. Baird, C. W. P. Palmer, D. N. Stacey, and G. K. Woodgate, *J. Phys. B* **20**, 3663 (1987).
- [18] J. Li, C. Nazé, M. Godefroid, S. Fritzsche, G. Gaigalas, P. Indelicato, and P. Jönsson, *Phys. Rev. A* **86**, 022518 (2012).
- [19] C. Nazé, S. Verdebout, P. Rynkun, G. Gaigalas, M. Godefroid, and P. Jönsson, *At. Data Nucl. Data Tables* **100**, 1197 (2014).
- [20] C. Nazé, E. Gaidamauskas, G. Gaigalas, M. Godefroid, and P. Jönsson, *Comput. Phys. Commun.* **184**, 2187 (2013).
- [21] E. Avgoustoglou, W. R. Johnson, D. R. Plante, J. Sapirstein, S. Sheinerman, and S. A. Blundell, *Phys. Rev. A* **46**, 5478 (1992).
- [22] A. N. Artemyev, V. M. Shabaev, and V. A. Yerokhin, *Phys. Rev. A* **52**, 1884 (1995).
- [23] K. Fahy, E. Sokell, G. O'Sullivan, A. Aguilar, J. M. Pomeroy, J. N. Tan, and J. D. Gillaspay, *Phys. Rev. A* **75**, 032520 (2007).
- [24] B. Blagojević, E.-O. Le Bigot, K. Fahy, A. Aguilar, K. Makonyi, E. Takács, J. N. Tan, J. M. Pomeroy, J. H. Burnett, J. D. Gillaspay *et al.*, *Rev. Sci. Instrum.* **76**, 083102 (2005).

- [25] R. Silwal, E. Takacs, J. M. Dreiling, J. D. Gillaspay, and Yu. Ralchenko, *Atoms* **5**, 30 (2017).
- [26] D. Osin, J. Reader, J. D. Gillaspay, and Yu. Ralchenko, *J. Phys. B* **45**, 245001 (2012).
- [27] A. Kramida, Yu. Ralchenko, J. Reader, and NIST ASD Team, NIST Atomic Spectra Database, version 5.7.1, <https://physics.nist.gov/asd>.
- [28] R. Katai, S. Morita, and M. Goto, *J. Quant. Spectrosc. Radiat. Transfer* **107**, 120 (2007).
- [29] J. D. Gillaspay, *J. Instrum.* **5**, C10005 (2010).
- [30] W. Borchers, E. Arnold, W. Neu, R. Neugart, K. Wendt, G. Ulm, and ISOLDE Collaboration, *Phys. Lett. B* **216**, 7 (1989).
- [31] I. Angeli and K. P. Marinova, *At. Data Nucl. Data Tables* **99**, 69 (2013).
- [32] G. Fricke and K. Heilig, *Nuclear Charge Radii*, edited by H. Schopper (Springer, Berlin, 2004).
- [33] J. Libert, B. Roussi ere, and J. Sauvage, *Nucl. Phys. A* **786**, 47 (2007).
- [34] W. Fischer, H. H uhnermann, G. Kr omer, and H. J. Sch afer, *Z. Phys.* **270**, 113 (1974).